An extra-heating mechanism in Doppler-cooling experiments

Thierry Chanelière, Jean-Louis Meunier, Robin Kaiser, Christian Miniatura, David Wilkowski

An extra-heating mechanism in Doppler-cooling experiments

T. Chanelière,[1] J.-L. Meunier,[1] R. Kaiser,[1] C. Miniatura,[1] and D. Wilkowski[1]

[1] *Institut non linéaire de Nice, UMR 6618 du CNRS, 1361 route de Lucioles, F-06560 Valbonne, France.*

(Dated: December 18, 2004)

In this paper we experimentally and theoretically investigate laser cooling of Strontium 88 atoms in one dimensional optical molasses. In our case, since the optical cooling dipole transition involves a $J_g = 0$ groundstate, no Sisyphus-type mechanisms can occur. We are thus able to test quantitatively the predictions of the Doppler-cooling theory. We have found, in agreement with other similar experiments, that the measured temperatures are systematically larger than the theoretical predictions. We quantitatively interpret this discrepancy by taking into consideration the extra-heating mechanism induced by transverse spatial intensity fluctuations of the optical molasses. Experimental data are in good agreement with Monte-Carlo simulations of our theoretical model. We thus confirm the important role played by intensity fluctuations in the dynamics of cooling and for the steady-state regime.

PACS numbers: PACS: 32.80.Pj

I. INTRODUCTION

Initiated in the mid-seventies, laser cooling, trapping and manipulation of atoms rapidly became a very successful field of research [1], culminating twenty years later with the observation of Bose-Einstein condensation of alkali atoms [2]. This success story begun with the seminal Doppler cooling theory which was designed for two-level systems [3, 4]. However, the first reliable tests of the Doppler theory could only be performed at the end of the eighties. As it turned out, the measured temperatures in the experiments were *well below* the predicted Doppler values [5]. This surprising results indicated that another much more efficient cooling mechanism was at work in the experiments. This mechanism, now known as Sisyphus cooling, was identified soon after [6]. The key point was to understand that internal groundstate degeneracies were opening the way to a new cooling mechanism based on optical pumping in the presence of polarization gradients. This cooling mechanism is now the basic ingredient for most experiments in the field and thus gave the Doppler theory a more academic status.

Recent laser technological advances however opened the way to cooling and trapping experiments with earth-alcaline and rare-earth atoms (Calcium Ca, magnesium Mg, strontium Sr and Ytterbium Yb). As these atoms exhibit a zero spin groundstate, Sisyphus cooling is absent. Interest in testing the Doppler theory to gain better control on achievable temperatures has thus been renewed. To our knowledge, all experiments on laser cooling of these atoms [7, 8, 9, 10] always reported much larger temperatures than the Doppler theory prediction. This is a strong clue in favor of an extra-heating mechanism still to be clearly identified. Approaching the Doppler limit in magneto-optical traps (MOT) operating with earth-alcaline atoms seems a challenge and a better understanding of this heating mechanism is required for future experimental improvements. To our knowledge only one explanation has been published to understand these high temperatures [11]. The argumentation is based on heating induced by inelastic collisions. However, as the authors themselves show, this heating mechanism sets in only for atomic densities much higher than for those measured in typical MOT ($10^9 - 10^{11}$atoms/cm^3). For this reason this explanation fails to understand the results presented in this paper and also in all previously cited publications.

Heating mechanisms depending on the density and/or the number of atoms in the cold MOT cloud are well known even for degenerate groundstate atoms [12]. They essentially rely on reabsorption of scattered photons in the cold MOT [13]. This situation is encountered as soon as light multiple scattering sets in, *i.e.* when the light scattering mean free path ℓ is comparable to the MOT size L. Similar multi-atoms and multi-photons effects certainly also exist with earth-alcaline MOTs, but they can be made negligible by working at low densities ($n \approx 2.5\,10^9$atoms/cm^3) and at low optical thickness ($b = L/\ell \approx 0.3$ at resonance).

Strictly speaking, Doppler theory can also be tested with degenerate atoms provided a suitable molasses polarization configuration is chosen [14]. Indeed, for 1D-cooling with parallel polarizations ($\sigma^+ - \sigma^+$ or $\pi - \pi$ configurations), no Sisyphus cooling can occur. However, even in this case, the authors found unusual high temperatures. They suggested that this discrepancy was due to molasses intensity imbalance, leading to a local drift of the atomic average velocity in the cloud. We agree with this explanation as we will show in detail in this paper.

We have performed specific temperature measurements on ^{88}Sr (Sr in short hereafter) in a 1D-cooling configuration. This is the ideal situation to test the Doppler theory for two reasons. First, we induce cooling on a $J_g = 0 \rightarrow J_e = 1$ atomic optical transition. Second, 2D or 3D Doppler cooling would be more difficult to analyze quantitatively. Indeed

interference between the six laser MOT beams can induce light shifts modulations, leading to modifications of the usual friction and diffusion coefficients [15]. These spurious effects do not exist in 1D configuration with mutual orthogonal polarized counter-propagating laser beams. The new important ingredient here is that we incorporate in the original Doppler theory the effect of *transverse spatial intensity fluctuations of the laser molasses profiles.*

The paper is organized as follows: after some details about the experimental procedure, we compare velocity dispersion measurements with the Doppler theory predictions (section II). We have found temperatures 10 times larger than predicted. Indeed, at a laser detuning $\delta = -\Gamma/2$, we have measured a velocity dispersion $\sigma_v = 0.7 \pm 0.2\, m/s$ ($T \approx 5\, mK$) whereas the Doppler theory predicts $\sigma_v = 0.23\, m/s$ ($T \approx 0.5\, mK$). In section III, we will show, on very general arguments, why the molasses transverse intensity fluctuations heat the cold cloud. We then derive an analytical model valid in two limiting cases: when the transverse distance $L_\perp$ travelled by an atom during the longitudinal velocity damping time is much shorter or much longer than the transverse correlation length ξ_s of the molasses intensity fluctuations. As expected, these two different limits give rise to different final velocity distributions. In subsection III D, we will compare our results to a Monte-Carlo simulation. Most of our experimental data correspond to $L_\perp \ll \xi_s$. In this case, the dynamics of the velocity distribution shows an unusual behavior. The velocity dispersion σ_v is first reduced by the friction force and then increases after a time scale related to ξ_s (section IV). This specific behavior confirms the dominant role played by the transverse intensity fluctuations in 1D-cooling with a $J_g = 0 \rightarrow J_e = 1$ transition.

II. EXPERIMENTAL RESULTS

A. Magneto-optical trap

The cold strontium cloud is produced in a MOT. The $J_g = 0 \rightarrow J_e = 1$ dipole transition under consideration is the optical atomic line ${}^1S_0 - {}^1P_1$ at $\lambda = 461\, nm$. The excited-state natural linewidth is $\Gamma/2\pi = 32\, MHz$ and the corresponding saturation intensity is $I_s = 42.5\, mW/cm^2$. First an effusive Sr beam is extracted from a $500^\circ C$ oven. Then a $27\, cm$ long Zeeman slower reduces the Sr longitudinal velocity within the velocity capture range of the MOT ($\sim 50\, m/s$). The Zeeman slower, MOT, and probe laser beams operate at $461\, nm$ and are generated from the same frequency-doubled source detailed in [16]. Briefly, a single-mode grating stabilized diode laser and a tapered amplifier are used in a master-slave configuration to produce $500\, mW$ of light at $922\, nm$. This infrared light is then frequency-doubled in a semi-monolithic standing-wave cavity with an intra-cavity $KNbO_3$ nonlinear crystal. The cavity is resonant for the infrared light while the second harmonic exits through a dichroic mirror providing $150\, mW$ of tunable single-mode light, which is then frequency locked on the $461nm$ Sr line in a heat pipe. We use acousto-optic modulators for subsequent amplitude and frequency variations. The MOT is made of six independent trapping beams. Each beam is carrying an intensity of $5.2\, mW/cm^2$ and each beam waist is $8\, mm$. The trapping beams are red-detuned by $\delta = -\Gamma$ with respect to the atomic resonance. Two anti-Helmoltz coils generate a $70\, G/cm$ magnetic field gradient to trap the atoms. The number of trapped atoms, as deduced from fluorescence measurements, is $N \approx 2.5\, 10^6$. The (Gaussian-shaped) cloud dispersion is roughly $0.6\, mm$. The velocity dispersion of atoms in the MOT is typically $\Delta v \sim 1\, m/s$. Technical details about temperature measurements are given in the following section.

B. 1D-cooling and time-of-flight measurements

In addition to the previously discussed experimental set-up (MOT, Zeeman slower), two additional contra-propagating laser beams are used to perform a 1D molasses (see figure 1). These 1D cooling beams are located in the horizontal plane. Some quarter-wave and half-wave plates are used to fix the relative polarizations of the two contra-propagating laser beams. An acousto-optical modulator in a double-pass configuration is used to adjust the laser frequency from resonance down to $-\Gamma$. The same acousto-optical modulator is used to control the laser intensity up to I_s. The beam waist is $3.5\, mm$ at the cold cloud position, thus much bigger than the MOT size.

The time sequence of the experiment is generated by a personal computer with digital output ports dedicated to this task. An internal clock updates and synchronizes the digital output ports every $10\, \mu s$. This elementary time step is short enough for our purposes. The digital output ports are connected to switches which turn on and off the lasers beams (rising and falling times shorter than $1\, \mu s$), the magnetic field (rising time of few ms and falling time of $100\, \mu s$) and the CCD camera chopper (opening and closing times of $200\, \mu s$). The time sequence is designed as follows: first the MOT is operated during about $20\, ms$. Then the MOT lasers and magnetic gradient are switched off. The 1D-molasses laser beams are then switched on during $500\, \mu s$. This cooling time is appropriately chosen : atoms reach the cooling steady-state regime while, at the same time, the expanding atomic cloud remains smaller than the cooling beams size. After the 1D-cooling sequence, the temperature of the cold cloud is extracted from a time-of-flight (TOF)

measurement technique. For this purpose, all the laser beams are switched off and the cold cloud expands ballistically in the dark. The duration of the dark period is varied from a few $100\,\mu s$ up to $1.5\,ms$. Then a fluorescence image of the expanding cloud is recorded on a CCD camera by briefly switching on the MOT beams during $20\,\mu s$. The whole time sequence is then repeated as long as necessary to obtain a good signal-to-noise ratio (see figure 1).

Figure 2 shows three images of the cloud after different ballistic expansion times. The elliptical shape of the cloud is a signature of the 1D-cooling sequence. Indeed the cooling axis is precisely the small axis of the ellipse. This dimension will be thereafter referenced as the *longitudinal* axis. In the two other dimensions, thereafter referenced as the *transverse* axes, the cloud is heated by random spontaneous emission. From these images, we extract the dispersion of the longitudinal *spatial* distribution of atoms in the cloud, integrated over the transverse directions. Because of the finite size of the image, we cannot have access to the long tail of the spatial distribution. Hence, we truncate all recorded distributions at 2% of their maximum value. Assuming the initial atomic positions and velocities in the MOT to be uncorrelated and centered, the ballistic time evolution of the spatial dispersion is simply $\sigma_x^2(t) = \sigma_x^2(0) + \sigma_v^2\, t^2$. The velocity dispersion $\sigma_v = \sqrt{\langle v^2 \rangle}$ is then easily extracted from the experimental data. To cross-check these measurements, we have also used a different measurement method, namely a spectroscopic technique. It consists in probing the cold cloud with an ultra-stable laser beam tuned on resonance with the $^1S_0 - {}^3P_1$ Sr transition line (note that this is also a $0 \rightarrow 1$ transition). Because this line is spin-forbidden, its frequency width is very small ($7.5\,kHz$) and is thus Doppler-broadened in the MOT [17]. Hence, we have a direct access to the velocity distribution by measuring the Doppler-induced spectral width. We have checked that these two different techniques give the same results, thereby confirming the validity of the TOF measurements, easier to handle, and for this reason routinely used in this experiment for temperature measurements.

C. Doppler theory and results

Doppler theory is based on absorption-fluorescence cycles which induce a cooling mechanism competing with a heating mechanism. Cooling is due to a mean friction force $F = -m\gamma v$ which damps the velocity and heating is due to a Langevin fluctuating force F_ν (photon noise) giving rise to diffusion with constant D *in velocity space*. At equilibrium these processes exactly balance (fluctuation-dissipation theorem) and the Doppler temperature is found to be $k_B T_D = m\,\sigma_D^2 = m\,D/\gamma$. All experimental data presented in this paper have been obtained in the $lin \| lin$ polarization configuration. In this case, analytical expressions for the damping coefficient γ can be found in [18] and in [5] for the diffusion constant D. The analytical expression of the Doppler variance at low laser intensities I and *negative* detuning δ is then

$$\sigma_D^2 = \frac{D}{\gamma} \approx \frac{7}{20}\,\frac{\hbar\Gamma}{m}\,\frac{1+\Delta^2}{2|\Delta|}\,\left(1 + \frac{2}{7}\,\frac{11+\Delta^2}{(1+\Delta^2)^2}\,s_0\right) = \sigma_0^2(\Delta)\,(1 + 2\beta(\Delta)\,s_0) \tag{1}$$

Here $\Delta = 2\delta/\Gamma$ is the laser detuning in units of $\Gamma/2$ and $s_0 = I/I_s$ is the on-resonance saturation parameter. As could have been guessed, the Doppler temperature is related to the only energy scale of the problem, namely the excited-state energy width $\hbar\Gamma$. We thus see that, at low intensities, $\sigma_D \approx \sigma_0(\Delta)\,(1+\beta(\Delta)s_0)$ grows linearly in s_0 with slope $\beta(\Delta)\sigma_0(\Delta)$ from $\sigma_0(\Delta)$. Minimization of $\sigma_0(\Delta)$ is achieved for $\Delta = -1$ and gives $\beta = 3/7$, $\sigma_0 = \sqrt{7\hbar\Gamma/20m} \approx 0.23\,m/s$.

In the strict 1D Doppler theory, the final velocity distribution and the corresponding temperature should depend on the polarization configuration. For example, in the $lin \| lin$ polarization channel, photon redistribution processes between the two contra-propagating laser fields can occur, whereas they are forbidden in the $lin \perp lin$ polarization channel. Hence, the polarization configuration affects both friction and diffusion. We have tested different polarization configurations ($lin \| lin$, $lin \perp lin$ and $\sigma^+ - \sigma^-$) but no significative temperature modifications have been found in the parameters range used in this experiment (see below).

Figure 3 shows the experimental variation of the velocity dispersion σ_v as a function of Δ at low intensity ($s_0 = 0.08$). The global behavior is the same as the one predicted by the Doppler theory but systematically higher. For example, at $\Delta = -1$, we get $\sigma_v = 0.7 \pm 0.2\,m/s$ ($T \approx 5\,mK$) whereas the Doppler theory predicts $\sigma_v \approx \sigma_0 \approx 0.23\,m/s$ ($T \approx 0.5\,mK$). The mismatch is even more pronounced at small detuning and tends to be reduced at high detuning. Figure 4, obtained at $\Delta = -1$, shows a strong linear increase of σ_v as a function of s_0. The measured slope is $0.9\,m/s$ whereas the Doppler theory only predicts $0.1\,m/s$.

The on-resonance optical thickness corresponding to the data in figures 3 and 4 is typically $b \approx 0.3$ when the experimental sequence starts. At the end of the sequence, because the atomic cloud expands, $b \approx 0.15$. These optical thicknesses are not sufficiently low to discard multiple scattering effects (this would require $b \ll 1$). The role of multiple scattering of light is two-fold. First, it induces photon reabsorption leading to an average repulsion force and heating. However at $b \approx 0.3$, heating, as observed in [12], can here be neglected. Second, it implies beam

attenuation (Lambert-Beer law). This means that the average optical force is weaker for atoms located deep in the cloud and we get, as a net effect, an average compression force. In a MOT, these compression and repulsion forces are equilibrated by the trapping force [19]. This is not the case in optical molasses. In a 1D-molasses, the compression force is expected to dominate over the repulsion force induced by photon reabsorption, at least at moderate optical thicknesses. A quantitative estimate of multiple scattering effects is thus not easy. For example, in our case, the Lambert-Beer law predicts a maximum relative intensity imbalance of approximately 23% at low intensity, which is not negligible. However our experimental results strongly suggests that multiple scattering velocity inhomogeneous broadening is small. Indeed, as s_0 is increased, the optical thickness decreases since the scattering cross-section is reduced. The compression force is thus decreased and cannot explain the strong increase of σ_v *vs* s_0 evidenced in figure 4. Furthermore, multiple scattering induces some correlations between position and velocity which should alter the cloud ballistic expansion. This has not been observed in figure 2. As an ultimate test, we have change the number of atoms in the MOT by a factor 3 without detecting any modification of σ_v.

III. COOLING WITH INTENSITY IMBALANCE

We analyze in this section how *spatial stationary* transverse intensity fluctuations can modify the Doppler cooling predictions in a quantitative way. Starting from the analytical expression of the average force in 1D molasses, we take into account these spatial intensity fluctuations and we derive analytical results in two limiting cases, namely when cooling is achieved before intensity fluctuates and in the opposite case. This analytical model neglects the photon noise encapsulated in the Langevin force F_ν leading to a nonzero Doppler temperature. However, for a quantitative comparison with experimental data, we have developed a Monte-Carlo simulation which fully takes into account all fluctuating mechanisms (molasses intensity fluctuations *and* photon noise). These results will be detailed in subsections III C and III D.

A. Origin of spatial intensity imbalance

In the standard Doppler theory, the molasses beams are described as perfect plane waves. In real experiments however, the beams have a Gaussian-shaped transverse profile. Usually one can ignore the transverse dimensions of the beams because they are generally much larger than the MOT size. Nevertheless, the transverse intensity profiles are not defect-free ideal Gaussian profiles. Indeed, even starting from diffraction-limited laser beams, imperfections of optics elements (dust, aberrations, *etc*) induce scattering which generates an intensity speckle. Of course, in well-controlled experiments, this speckle pattern remains relatively small compared to the average beam intensity, but those two fields add coherently. In our experiment, we have measured the laser beam spatial transverse fluctuations by placing a CCD camera at the approximative position of the MOT. Subtracting the ideal Gaussian profile, we have computed the intensity fluctuations histogram (see figure 5). We found a Gaussian histogram with a relative standard deviation (with respect to the average intensity) in the range $10-20\%$.

The 1D-molasses is created by two contra-propagating beams issued from the same source. However, the speckle intensity generated by the optics imperfections in each arm are independent. It is thus reasonable to consider, at each transverse position in the beam profile, the intensities $I_i\,(i=1,2)$ of the two molasses beams to be random *independent* Gaussian variables. Noting by s_i the corresponding on-resonance saturation parameters, we assume the probability distribution $\mathcal{P}(s_i)$ to be the same for the two beams. Hence the (common) first two moments, at each transverse position, are $\langle s_i\rangle = s_0$ and $\sigma_s^2 = \langle (s_i-s_0)^2\rangle$ $(i=1,2)$. In the following we will characterize the molasses intensity fluctuations by the ratio $r_s = \sigma_s/2s_0$. From experimental data, we have r_s in the range $5-10\%$. Another important feature is the transverse spatial correlation function (assumed to be the same for each beam), namely $\mathcal{C}(\mathbf{r}) = \langle s_i(\mathbf{r}')\, s_i(\mathbf{r}'+\mathbf{r})\rangle\,(i=1,2)$. The characteristic decay length of $\mathcal{C}(\mathbf{r})$ defines the transverse correlation length ξ_s. Strictly speaking, because of diffraction effects, ξ_s cannot be zero. We have experimentally found ξ_s to be of the order of few tenth of μm ($\xi_s = 30\mu m$ for the example shows in figure 5).

B. Analytical model

For a $0\rightarrow 1$ transition in the $lin\|lin$ configuration, atoms are modelled by a two-level system involving the same Zeeman states for each molasses beam. The two beams have the *same* red-detuned frequency ($\delta<0$), *opposite* wave-vector $\mathbf{k}$ but locally *different* saturations which fluctuate independently across the transverse profile of the beams but with the *same* correlation length ξ_s. The mean local radiation pressure force experienced by a single atom, with

longitudinal velocity v, takes the simple following form:

$$F = m\frac{v_R\Gamma}{2}\left[\frac{s_1}{1+s_1+s_2+(\Delta-2kv/\Gamma)^2}-\frac{s_2}{1+s_1+s_2+(\Delta+2kv/\Gamma)^2}\right] \quad (2)$$

$$\approx m\frac{v_R\Gamma}{2}\left[\frac{s_1}{1+2s_0+(\Delta-2kv/\Gamma)^2}-\frac{s_2}{1+2s_0+(\Delta+2kv/\Gamma)^2}\right] \quad (3)$$

where $v_R = \hbar k/m$ is the recoil velocity ($\approx 6\,mm/s$ for Sr). We have here assumed that the mechanical actions of the two laser beams can be added independently, only considering the total saturation of the optical transition to be (s_1+s_2). We have furthermore replaced (s_1+s_2) by $2s_0$ in the denominator. A more careful analysis, along the lines given below, shows that this is indeed valid with our experimental parameters.

Near the steady state, the Doppler broadening become negligible, $kv \ll (\Gamma, \delta)$ and the force can be safely approximated by:

$$F \approx -m(s_1+s_2)\gamma_v\, v + m(s_1-s_2)\, a \quad (4)$$

$$\approx -2ms_0\gamma_v\, v + m(s_1-s_2)\, a \quad (5)$$

Defining the recoil angular frequency $\omega_R = 2\pi\,\nu_R = \hbar k^2/2m$ ($\nu_R \approx 10.6\,kHz$ for Sr), we have

$$\gamma_v = \omega_R\,\frac{4|\Delta|}{(1+\Delta^2+2s_0)^2} \quad \text{and} \quad a = \frac{v_R\Gamma}{2}\,\frac{1}{1+\Delta^2+2s_0} \quad (6)$$

The friction force is given by the term proportional to v and gives rise to a mean damping time:

$$\tau_v = (2s_0\gamma_v)^{-1} \quad (7)$$

Consider now an atom moving across the molasses beams with transverse velocity $v_\perp$. This velocity is unaffected by the longitudinal cooling. So, as the atom flies across the beam, it may experience *induced temporal* molasses intensity fluctuations. The induced *correlation time* of these fluctuations is simply

$$\tau_s = \xi_s/v_\perp \quad (8)$$

We have thus two competing dynamical processes, the cooling one with characteristic time τ_v and the intensity random (induced) temporal variations with correlation time τ_s. The global velocity dynamics can be easily analyzed when these time scales are well separated.

1. *The regime $\tau_v \ll \tau_s$*

For atoms fulfilling this condition, the damping process is completed before intensities fluctuate. Then the constant force and the friction coefficient in (4) can be considered as time-independent. Atoms thus behave as if $v_\perp$ was zero. However, because ξ_s is much shorter than the cloud size, each atom experiences randomly fixed distributed intensity imbalances and, in turn, a random constant force. The random stationary velocity is $v_\infty = a\tau_v(s_1-s_2)$. It is Gaussian-distributed with zero mean and dispersion

$$\sigma_\infty = \sqrt{2}a\tau_v\,\sigma_s = \sqrt{2}\,\frac{\Gamma}{k}\,\frac{1+|\Delta|^2+2s_0}{4|\Delta|}\,r_s \quad (9)$$

To find the final velocity distribution, one has to incorporate the photon noise force F_ν. As the photon noise and intensity fluctuations are independent, the total velocity variance is the sum of the Doppler and intensity variances $\sigma_v^2 = \sigma_D^2 + \sigma_\infty^2$. In this regime, intensity fluctuations thus give rise to an extra-heating mechanism inducing an inhomogeneous broadening of the Doppler velocity distribution. At $\Delta = -1$, s_0 small and $r_s = 9\%$, one gets $\sigma_\infty \approx 0.94\,m/s$ and $\sigma_v \approx 0.97\,m/s$.

2. *The regime $\tau_v \gg \tau_s$*

In this regime, the molasses intensities fluctuate wildly before the atom reaches its stationary state. Thus they cannot be treated as time-independent quantities. They can however be treated as independent *Markovian* (short

memory) processes. From the expression (4) of the total force, we derive the following master equation for the velocity distribution $\mathrm{P}_t(v)$ [20] (details will be given elsewhere):

$$\mathrm{P}(v, t+\tau_s) = \int \mathrm{d}s_1\, \mathrm{d}s_2\, \mathrm{d}v'\, \mathcal{P}(s_1)\, \mathcal{P}(s_2)\, \mathrm{P}(v', t)\, \delta\left(v - v' - \frac{F}{m}\tau_s\right) \tag{10}$$

In this equation, at each time step τ_s, the saturations s_1 and s_2 take on new values uncorrelated with the previous ones.

One should note that we have kept here both the *additive* noise, given by the $(s_1 - s_2)$ term, and the *multiplicative* noise, given by the $(s_1 + s_2)v$ term. This last term had been replaced by $2s_0 v$ in our previous analysis (expression (5) of the force). In the limit of small velocity changes at the elementary time scale τ_s, one can derive from (10) a Fokker-Planck type equation (see Appendix VII):

$$\frac{\partial \mathrm{P}(v,t)}{\partial t} = \frac{1}{\tau_v}\frac{\partial}{\partial v}(v\mathrm{P}(v,t)) + \frac{\partial^2}{\partial v^2}(D(v)\mathrm{P}(v,t)) \tag{11}$$

Defining $D_\infty = \sigma_\infty^2/2\tau_v$, the velocity-dependent diffusion constant has the following expression:

$$D(v) = D_\infty\, \left[1 + (1+2r_s^2)\,[v/\sigma_\infty]^2\,\right]\, \frac{\tau_s}{\tau_v} \approx D_\infty\, \left[1 + (v/\sigma_\infty)^2\right]\, \frac{\tau_s}{\tau_v} \tag{12}$$

since generally $2r_s^2 \ll 1$. This velocity-dependence originates from the multiplicative noise and leads to abnormal diffusion. The stationary velocity distribution P_0 is then easily found to take the following form ($\mathcal{N}$ is a normalization constant):

$$\mathrm{P}_0(v) \approx \mathcal{N}\,[1 + (v/\sigma_\infty)^2]^{-(1+\eta)} \tag{13}$$

where $\eta = \tau_v/\tau_s \gg 1$. The full width at half maximum of this distribution is

$$\Gamma_v = 2\sqrt{\ln 2}\,\sqrt{\frac{\tau_s}{\tau_v}}\,\sigma_\infty \;\ll\; \sigma_\infty \tag{14}$$

As easily checked $D(v) \approx D_\infty\, \tau_s/\tau_v$ for $v \sim \Gamma_v$. Hence the impact of abnormal diffusion is in fact negligible when $\tau_v \gg \tau_s$ and the velocity distribution is very close to a Gaussian with velocity dispersion

$$\sigma_v \sim \sqrt{\frac{\tau_s}{\tau_v}}\,\sigma_\infty \ll \sigma_\infty \tag{15}$$

which is much narrower than the velocity dispersion found in the long correlation limit (9) by the factor $\sqrt{\tau_s/\tau_v}$.

Figure 6 shows σ_v as a function of r_s in the long and short correlation time limits ($\Delta = -1$, $s_0 \ll 1$). When $r_s \to 0$, σ_v goes to zero in both limits. This does not mean that the temperature goes to zero in experiments. Indeed, in the previous discussion we have discarded the photon noise at the physical origin of the bare Doppler theory. Its contribution at low saturation is given by the dotted line in figure 6. We can see that the noise induced by long correlation times starts to dominate at $r_s > 2.5\%$, a fairly small value. Hence, to achieve cooling up to the Doppler limit at $\Delta = -1$, one has to minimize the ratio τ_c/τ_v for a fixed value of r_s. This can be done in different ways. First, by decreasing the laser intensity to increase τ_v. Second, by decreasing τ_s. As shown by (8), this can be achieved either by avoiding large transverse intensity defects in the laser profiles to decrease the correlation length ξ_s or by increasing $v_\perp$. This is indeed was has been observed in atomic beam experiment [21] where temperatures very close to the Doppler limit had been found along one *transverse* dimension.

In a MOT, if the fluctuations of the transverse intensities are not the same for all three dimensions, the temperature is expected to be anisotropic. Moreover coupling mechanisms occur between the cooling dimensions. Thus high velocity dispersion along one dimension tends to reduce the temperature in the orthogonal plane. In our 1D-molasses, the transverse velocity is fixed by the initial MOT sequence and τ_s/τ_v is usually bigger than 1. As we will see in Section III.D., this means that transverse intensity fluctuations are the major heating mechanism.

C. Monte-Carlo simulations

In order to quantitatively test our theory and not relying on questionable approximations, we have developed a Monte-Carlo (MC) simulation. This MC simulation fully takes into account the photon noise leading to the Doppler

cooling limit, saturation of the transitions and the transverse intensity fluctuations discussed so far, *i.e.* with *arbitrary* correlation time τ_s and saturation dispersion σ_s.

The shortest time scale in the MC calculation is given by the excited-state lifetime $\tau_e = 1/\Gamma$. To mimic the transverse flight of atoms, the molasses saturation fluctuations $\delta s_i = (s_i - s_0)$ $(i = 1, 2)$ become time-dependent parameters and evolve according to the damped random path discrete equation (n labels the number of time steps τ_e)

$$\delta s_i(n+1) = (1-\rho)\,\delta s_i(n) + R_n \tag{16}$$

with $\rho \ll 1$. The first term in this equation is the friction term, relaxing saturation to its stationary value s_0, while the last term is a random variable, with zero mean value, uniformly distributed over the range $[-\epsilon/2, \epsilon/2]$. A simple calculation shows that $\langle R_n^2 \rangle = \epsilon^2/12$. We further assume that the R_n's are decorrelated. The continuous limit of (16) is

$$\frac{d\,\delta s_i}{dt} + \frac{\rho}{\tau_e}\,\delta s_i = R(t) \tag{17}$$

As the correlation time τ_s should correspond to the damping time of this equation, we see that $\rho = \tau_e/\tau_s$. Thus fixing τ_s fixes ρ in (16). The last term of (17) is a δ-correlated Langevin term with zero mean. Its time-correlation function is $\langle R(t')R(t)\rangle = 2\mathcal{D}\,\delta(t-t')$ where it is easily shown that $\mathcal{D} = \epsilon^2/24\tau_e$. The fluctuation-dissipation theorem then dictates $\sigma_s^2 = \mathcal{D}\tau_s$, leading to

$$\epsilon = 2\sqrt{6\rho}\,\sigma_s \tag{18}$$

This last result can be found more elegantly by squaring (16) and averaging over the probability distribution of R_n. Hence experimental determination (or convenient choice) of the macroscopic ingredients τ_s and σ_s fixes in principle the microscopic ingredients ϵ and ρ in (16).

Figure 7 shows the obtained final velocity dispersion σ_v as a function of τ_s/τ_v for $s_0 = 0.04$ and $r_s = 9\%$. The velocity damping time, calculated with (7), is $\tau_v = 200\,\mu s$. As expected, σ_v is higher for long correlation times $\tau_s \gg \tau_v$. When $\tau_s \sim \tau_v$, σ_v is very sensitive to τ_s. At lower values $\tau_s \ll \tau_v$, σ_v is minimum and, for these parameters, reaches the Doppler limit. The final distributions (not shown here) are quasi-Gaussian, even at small τ_s.

D. Quantitative comparison with experimental data

We have showed in section II.C that the measured velocity dispersion were always larger than the Doppler theory predictions. We now compare our experimental data with the results of our previous MC simulation. In order to stick as close as possible to the experiments, we also take into account the transverse velocity distribution (a centered Gaussian with dispersion $\Delta v_\perp \approx 0.8\,m/s$) in the MC simulation.

In figure 3 the solid curve corresponds to the MC simulation performed at $r_s = 9\%$ and $\xi_s = 60\,\mu m$. These quantities are fit-parameters in the MC simulation but remain in the range of the measured ones (see III A). As one can see, the agreement with experimental points is now very good, providing a clear understanding of the physics at work in the experiment. Coming back to (6), close to resonance, the friction term decreases while the intensity imbalance term increases. Hence, the mismatch between experiment and Doppler theory is maximal.

Again, an excellent agreement between MC simulation (solid curve) and data is found in figure 4. To properly understand these results, one has to remind that the cross-over region between the long- and short-correlation time limits is given by $\tau_s = \tau_v$, or equivalently by $s_0 = v_\perp/2\gamma_v\xi_s \sim 0.1$. TOF measurements before the molasses sequence have shown that $v_\perp \approx 0.8\,m/s$ whereas ξ_s is the chosen MC parameter. This is exactly what is seen in figure 4 and the Doppler theory is recovered when $s_0 \to 0$. However, this short-correlation time limit ($\tau_s \ll \tau_v$) was not experimentally accessible because the 1D-cooling duration sequence was not long enough to reach the steady state. This is why most of the data points correspond to the long-correlation time limit ($\tau_s \gg \tau_v$) and can be compared to (9). This is done in figure 4 where the dashed line corresponds to the prediction given by (9). The general behavior is correct, indicating that saturation of the atomic transition indeed plays a significant role. However the prediction (9) is a little bit too large. This is not surprising since, for the explored range of parameters, some atoms will always have sufficiently high transverse velocities to fulfill the short correlation time criterion, both in the experiment and in the MC simulation. As a consequence, the velocity dispersion σ_v will be reduced. In other words, (9) corresponds to a zero-transverse velocity case giving over-estimated predictions.

Figure 8 shows the longitudinal *spatial* distribution obtained for the longest ballistic time at $\Delta = -1$ and $s_0 = 0.08$. It is two times broader than the initial spatial distribution and essentially proportional to the velocity distribution.

We can then try to compare it to the velocity distribution obtained with the MC simulation (solid line). We have also plotted the Gaussian distribution expected from standard Doppler theory (dashed line). The actual non-Gaussian shape of the MC distribution is explained by the transverse velocity dispersion ($\Delta v_\perp \approx 0.8\, m/s$). For each *fixed* transverse velocity, the distribution is quasi-Gaussian with a width depending on $v_\perp$ (see figure 6 and discussions in Section III B). For this simple reason, summing over the transverse velocity distribution leads to a non-Gaussian distribution. The non-Gaussian shape of the MC simulation matches the experimental distribution better than the Gaussian one.

As a conclusion of this section, we again stress that we have quantitatively explained both the behavior of the velocity dispersion σ_v as a function of laser detuning and intensity and the observed non-Gaussian distributions. This puts strong evidence on the fundamental role played by molasses intensity defects in the cooling process.

IV. COOLING DYNAMICS

Figure 9 show the time evolution of σ_v for three different values of τ_c corresponding to the short, intermediate and long correlation time limit. When τ_s is short (or equivalently $v_\perp$ large), the corresponding curve (a) displays an exponential-type behavior decaying to the Doppler steady-state value. This curve is in agreement with the dashed line Doppler prediction. When τ_s is long (or equivalently $v_\perp$ small), the dynamics evidenced by curve (c) is more complex. First σ_v reaches a minimum value within a time scale corresponding to the damping time τ_v. Then, σ_v increases again and reaches the steady state value σ_∞ predicted by (9). When the mean velocity and the local intensity imbalance are uncorrelated in the initial state, then this long correlation time behavior is generic and does not depend anymore on the initial state. Because the intensity correlation length ξ_s is large, the heating mechanism takes also some time to build up and the initial velocity distribution starts first to shrink. This is easily explained by considering the dynamics induced by (4) for times shorter than τ_s where transverse intensity fluctuations are dynamically frozen. After a proper averaging over intensities fluctuations, the following analytic expression for $\sigma_v(t)$ is derived:

$$\sigma_v(t)^2 = (\Delta v^2 + \sigma_\infty^2)\exp(-2t/\tau_v) + \sigma_\infty^2(1-\exp(-t/\tau_v)) \tag{19}$$

where Δv corresponds to the initial longitudinal velocity dispersion. the small time expansion $t \ll \tau_v$ of this equation gives:

$$\sigma_v(t) \approx \Delta v\,(1 - t/\tau_v) \tag{20}$$

clearly evidencing the velocity spread narrowing at small times. We have experimentally tested this specific behavior. Once the MOT is loaded, we have switched off the cooling laser beams within a time window of variable duration τ_{dark}. This dark sequence must be long enough to allow atoms to travel over transverse distances larger than the correlation length ξ_s of intensity fluctuations. Then, once the cooling lasers are switched on again, any correlation between the mean atomic velocity and the local intensity imbalance is wiped out. We should thus observe the behavior predicted by curve (c) in figure 9. The velocity dispersion σ_v is measured after a time τ by the TOF technique (see section II). In figure 10(a), we plot σ_v as a function of τ after a dark period $\tau_{dark} = 0.5\, ms$. We reproduce nicely the corresponding theoretical prediction. First we observe a decrease of σ_v followed by an increase, up to the final value (which is here the same as the initial value). We also checked that the dark period has to be long enough, as evidenced in figure 10(b). When τ_{dark} is short enough (less than $1\, ms$), decorrelation between the mean atomic velocity and local intensity imbalances is not completed. When τ_{dark} is long enough (larger than $1\, ms$), complete decorrelation is achieved and the dark period no longer plays any role in the cooling dynamics.

For practical reasons, these experiments were done with the MOT (*i.e.* on an 3D-cooling configuration in the presence of the magnetic field gradient) whereas the MC simulations were done for a 1D-cooling scheme. This major difference does not allow for a quantitative comparison between theory and experiment. However, the qualitative agreement is pretty good. This result suggests that the dominant extra-heating mechanism in a MOT is the same as in 1D-molasses.

Because the velocity distribution always starts by a compression period, one could imagine a cooling strategy implementing suitable repetitions of dark time windows to achieve Doppler-limited cooling. This simple idea however is not easy to handle because complete decorrelation between initial atomic velocities and intensity imbalances during these dark windows is requested. As the cloud cools down, the duration of the subsequent dark periods has to be increased accordingly to maintain this decorrelation. Unfortunately, as soon as the cooling time becomes very long, spurious effects such as large cloud expansions, then have time to set in.

V. CONCLUSIONS

We have evidenced in this paper the important role played by transverse spatial intensity fluctuations in 1D laser cooling of zero spin groundstate atoms where no Sisyphus cooling can occur. For intensity imbalanced molasses beams, the total radiation pressure force decomposes, at small velocities, into a friction force and a constant force. The latter is at the root of an additional heating mechanism. These two forces essentially depend linearly on the molasses intensities. In the presence of sub-Doppler cooling mechanisms, the friction term becomes intensity-independent whereas the constant force remains proportional to the intensity [5, 22, 23]. Hence, with sub-Doppler cooling, the effect of intensity imbalances can be arbitrarily small and, in turn, does not play any significant role. This is completely different for Doppler cooling where this effect remains dominant in most experimental cases.

The cooling steady-state reached by the atoms depends sensitively on the ratio ζ between the correlation length of transverse intensity fluctuations and the transverse distance travelled by the atoms before reaching the steady-state. For small ζ, the transverse fluctuations can be modelled by a Langevin force inducing an additional heating mechanism. For large ζ, the equilibrium state is reached at frozen molasses intensities. Atoms at different transverse positions then probe all possible intensities imbalance. This averaging procedure mainly affects the final atomic velocity and induces an inhomogeneous broadening of the Doppler velocity distribution. The impact on the final temperature is more severe than in the small ζ regime. This is evidenced by our experimental data which mostly lie in the large ζ regime. It is however possible, in principle, to reach the small ζ regime by appropriately reducing the intensities of the cooling beams and get final temperatures closer to the Doppler limit.

The cooling dynamics also exhibits an unusual behavior in the large ζ regime : the atoms are first cooled down before being heated up. This specific feature is also found in our experiments, thus confirming the central role of transverse intensity fluctuations in Doppler cooling.

VI. ACKNOWLEDGMENTS

This research is financially supported by the CNRS (Centre National de la Recherche Scientifique) and the BNM (Bureau National de Métrologie) contract N° 03 3 005.

VII. APPENDIX : DERIVATION OF THE MASTER EQUATION

The Fokker-Planck type equation (11) is obtained by starting with the master equation (10):

$$\mathrm{P}(v,t+\tau_s) = \int \mathrm{d}s_1\,\mathrm{d}s_2\,\mathrm{d}v'\;\mathcal{P}(s_1)\,\mathcal{P}(s_2)\;\mathrm{P}(v',t)\,\delta(v-v'-\frac{F(s_1,s_2,v')}{m}\tau_s) \tag{21}$$

By Fourier transforming this equation with respect to v, we get:

$$\widetilde{\mathrm{P}}(q,t+\tau_s) = \frac{1}{\sqrt{2\pi}}\int \mathrm{d}s_1\,\mathrm{d}s_2\,\mathrm{d}v'\;\mathcal{P}(s_1)\,\mathcal{P}(s_2)\;\mathrm{P}(v',t)\;\exp[-iq(v'+\frac{F(s_1,s_2,v')}{m}\tau_s)] \tag{22}$$

We plug now expression (4) of the force in this equation to find:

$$\widetilde{\mathrm{P}}(q,t+\tau_s) = \frac{1}{\sqrt{2\pi}}\int \mathrm{d}v'\;\widetilde{\mathcal{P}}[q\tau_s(a-\gamma_v v')]\;\widetilde{\mathcal{P}}^*[q\tau_s(a+\gamma_v v')]\;\mathrm{P}(v',t)\exp(-iqv') \tag{23}$$

where the star denotes complex conjugation and where

$$\widetilde{\mathcal{P}}(u) = \int \mathrm{d}s\,\mathcal{P}(s)\exp(-ius) \tag{24}$$

is proportional to the Fourier transform of the molasses saturation distribution $\mathcal{P}$. As discussed in section III A, the distribution $\mathcal{P}$ is a Gaussian with mean s_0 and dispersion σ_s. A Taylor expansion of (23) up to second order in τ_s then leads to:

$$\tau_v\,\frac{\partial\widetilde{\mathrm{P}}(q,t)}{\partial t} \simeq \frac{1}{\sqrt{2\pi}}\int \mathrm{d}v'\left[i\,qv' - q^2\frac{\tau_s}{2\tau_v}[v'^2(1+2r_s^2)+2r_s^2\frac{a^2}{\gamma_v^2}\right]\;\mathrm{P}(v',t)\;\exp(-iqv') \tag{25}$$

An inverse Fourier transform then gives equation (11) once we note that $\sigma_\infty = \sqrt{2}r_s a/\gamma_v$ according to equation (9).

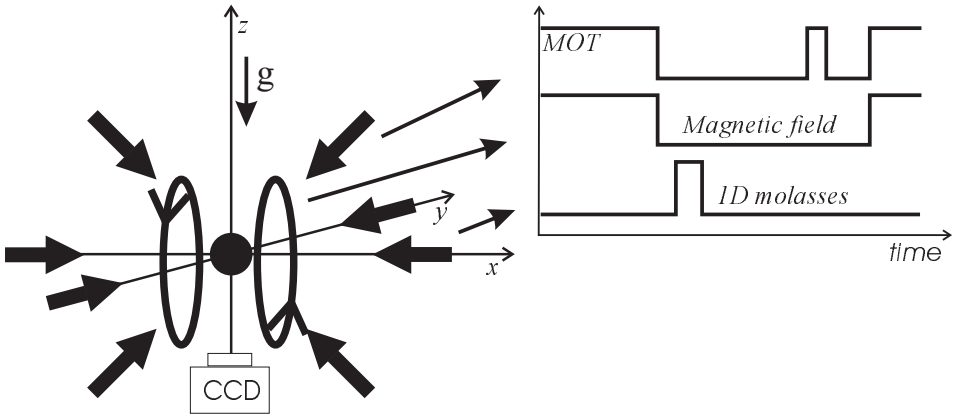

FIG. 1: Schematic drawing of our set-up and of the time sequence used in the experiment. The six independent MOT laser beams are along the x axis and ...sional cooling beams contrapropagate along the y ax... integrated over z.

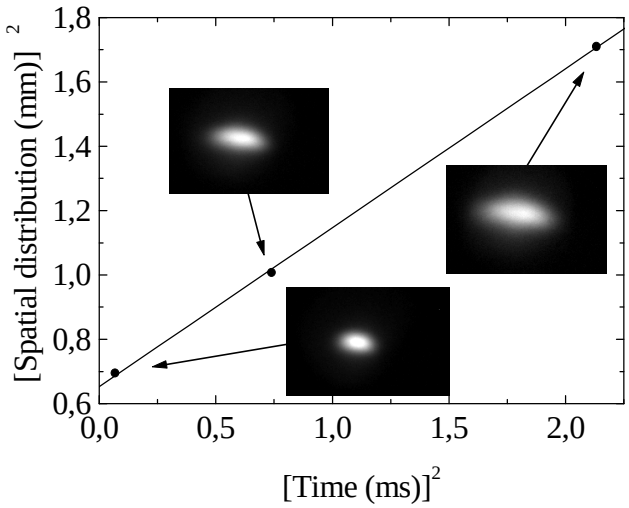

FIG. 2: After the 1D-cooling sequence along axis y, the spatial distribution in the horizontal plane is collected at three different ballistic expansion times by the time-of-flight technique. From these images, we extract the velocity dispersion σ_v in the cloud (see text).

[1] Fundamental systems in quantum optics, Les Houches LIII, Ed. J. Dalibard, J.M. Raimond and J. Zinn-Justin (North-Holland, Amsterdam, 1992).
[2] M.H. Anderson, J.R. Ensher, M.R. Matthews, C.E. Wieman, E.A. Cornell, Science **269**, 198 (1995); K. Davis, M.O. Mewes, M.R. Andrews, N.J. van Druten, D.S. Durfee, D.M. Kurn and W. Ketterle, Phys. Rev. Lett. **75**, 3969 (1995).
[3] T.W. Hansch and A.L. Schawlow, Opt. Comm. **13**, 68 (1975).
[4] D. J. Wineland and H. Dehmelt, Bull. Am. Phys. Soc. **20**, 637 (1975).
[5] P. Lett, W. Phillips, S. Rolston, C. Tanner, R. Watts and C. Westbrook, J. Opt. Soc. Am. B **6**, 2084 (1989).
[6] J. Dalibard and C. Cohen-Tannoudji, J. Opt. Soc. Am. B **6**, 2023 (1989); P. J. Ungar, D. S. Weiss, E. Riis and S. Chu, J. Opt. Soc. Am. B **6**, 2058 (1989)
[7] C.W. Oates, F. Bondu , and L. Hollberg, Eur. Phys. J. D **7**, 449 (1999).
[8] F. Loo, A. Brusch, S. Sauge, M. Allegrini, E. Arimondo, N. Andersen and J. Thomsen, J. Opt. B: Quantum Semiclass. Opt. **6**, 81 (2004).
[9] X. Xu, T. Loftus, M. Smith, J. Hall, A. Gallagher and J. Ye, Phys. Rev. A **66**, 011401 (2002); X. Xu, T. Loftus, J. Hall and J. Ye, J. Opt. Soc. Am. B **20**, 968 (2003).
[10] T. H. Yoon, *private communication*.
[11] J. Piilo, E. Lundh and K.-A. Suominen, Phys. Rev. A, **70**, 013410 (2004).

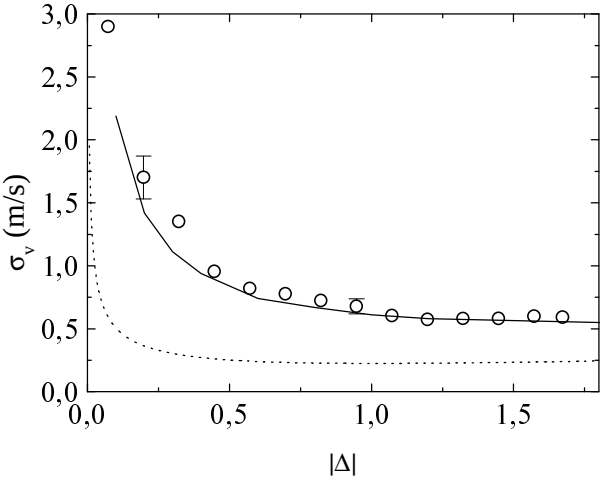

FIG. 3: Velocity dispersion σ_v as a function of $|\Delta| = 2|\delta|/\Gamma$ for $s_0 = I/I_s = 0.08$. The experimental data (circles) are compared to the Doppler prediction (dotted line) and to the Monte-Carlo simulation (solid line) at $r_s = 9\%$ and $\xi_s = 60\,\mu m$. As one can see the Doppler theory is completely off while very good agreement is obtained with our theoretical model (see text).

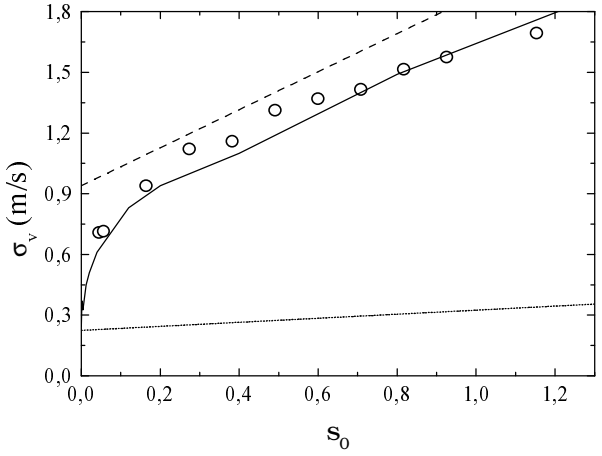

FIG. 4: Velocity dispersion σ_v as a function of the mean saturation parameter $s_0 = I/I_s$ at $\Delta = 2\delta/\Gamma = -1$. The experimental data (circles) are compared to the Doppler prediction (dotted line) and to the Monte-Carlo simulation (solid line) at $r_s = 9\%$ and $\xi_s = 60\,\mu m$. Whereas the Doppler theory is completely off, very good agreement is found with our theoretical model. The dashed line prediction corresponds to equation (9) (see text).

[12] M. Drewsen, P. Laurent, A. Nadir, G. Santerelli, A. Clairon, Y. Castin, D. Grison and C. Salomon, Appl. Phys. B **59**, 283 (1994).
[13] C. Cooper, G. Hillenbrad, J. Rink, C. Townsend, K. Zetie and C. Foot, EuroPhys. Lett. **28**, 397 (1994).
[14] D. S. Weiss, E. Riis, Y. Shery, P. J. Ungar and S. Chu, J. Opt. Soc. Am. B **6**, 2072 (1989).
[15] J. Dalibard, C. Cohen-Tannoudji, J. Phys. B: At. Mol. Phys. **18**, 1661 (1985).
[16] B. Klappauf, Y. Bidel, D. Wilkowski, T. Chanelière, R. Kaiser, Appl.Opt. **43** 2510 (2004).
[17] Y. Bidel, T. Chanelière, D. Wilkowski and R. Kaiser, in preparation.
[18] J. Gordon and A. Ashkin, Phys. Rev. A **21**, 1606 (1980).
[19] D. W. Sesko, T. G. Walker and C. E. Wieman, J. Opt. Soc. Am. B **8**, 946 (1991).
[20] N. G. Van Kampen, Stochastic progresses in physics and chemistry, North Holland Editor, 1981.
[21] A. Witte, Th. Kisters, F. Riehle and J. Helmcke, J. Opt. Soc. Am. B **9**, 1030 (1992).
[22] A. Steane, M. Chowdhury and C. Foot, J. Opt. Soc. Am. B **9**, 2142 (1992).
[23] J. Werner and H. Wallis, J. Phys. B: At. Mol. Opt. Phys. **26**, 3063 (1993).

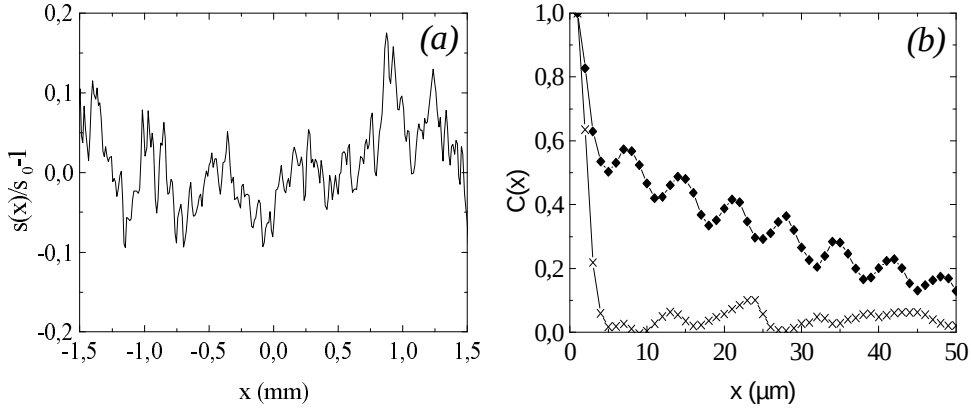

FIG. 5: Figure (a) shows typical relative intensity fluctuations of a laser beam once the smooth Gaussian profile is removed. The typical intensity dispersion is roughly 10% of the total signal. Figure (b) shows the spatial fluctuations correlation function $\mathcal{C}(x)$ *vs* a transverse coordinate. The transverse distance at which this correlation function vanishes defines the correlation length ξ_s. Experimentally we found $\xi_s \simeq 30\,\mu m$ (diamonds). The oscillation on top of the decay is due to the interference generated by the front window of the CCD camera. The fast decrease observed at short distances is also present when the laser is off (crosses). This fast decrease is thus due to the uncorrelated noise on the CCD camera and corresponds to the pixel size.

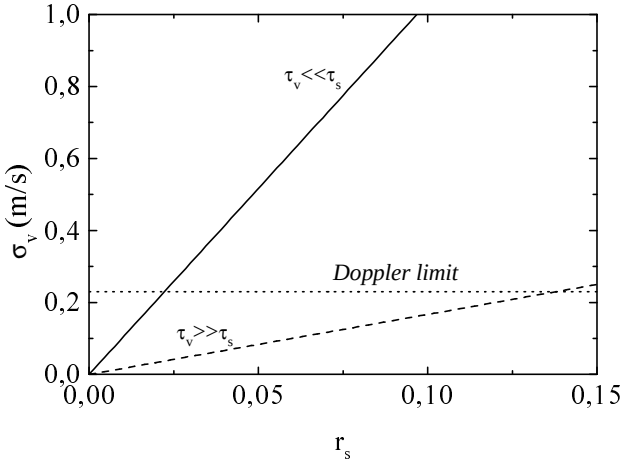

FIG. 6: velocity dispersion σ_v for the long (solid line) and short (dashed line) correlation time limit as a function of the relative fluctuation of the intensity $r_s = \sigma_s/2s_0$. In the short correlation time limit $\tau_s = 30\mu s$. The dotted line corresponds to the Doppler limit at low saturation and $\Delta = -1$ (see text).

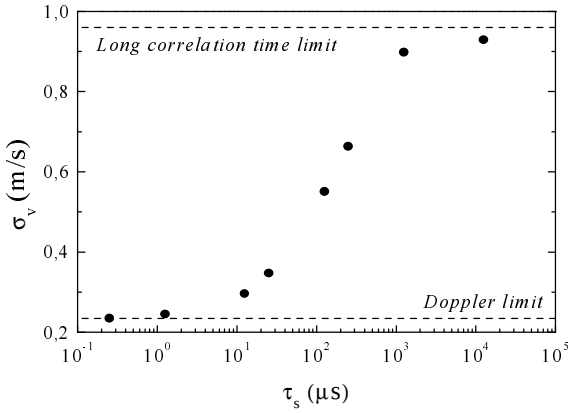

FIG. 7: Final velocity dispersion σ_v as a function of the correlation time τ_s (full circles). The transverse and longitudinal velocity dispersions are both equal to $\Delta v = 0.8\, m/s$. The mean saturation of each beam is $s_0 = 0.04$ and the saturation fluctuation parameter is $r_s = 9\%$. The upper dashed line represents the long correlation time limit while the lower one represents the Doppler-cooling limit (see text).

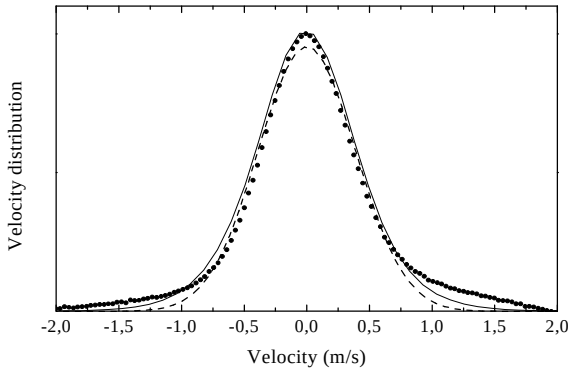

FIG. 8: Velocity distribution obtained at $s_0 = 0.08$ and $\Delta = -1$. Circles : experiment. Solid line : Gaussian fit. Dashed line : Monte-Carlo simulation with $r_s = 7.5\%$ and $\tau_s = 20\,\mu s$ (see text).

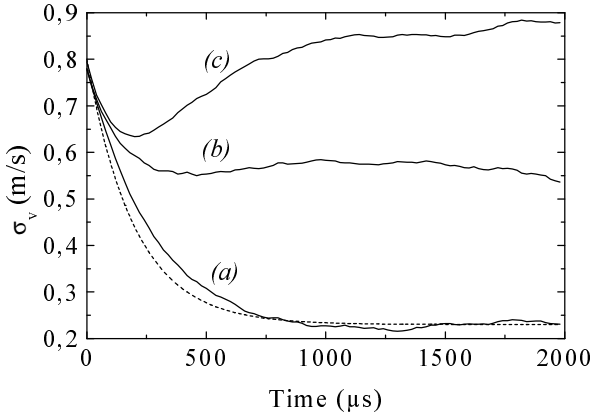

FIG. 9: Monte-Carlo simulations of the time evolution of the velocity dispersion σ_v for three characteristic correlation times: (a) short correlation time ($\tau_s = 1.25\,\mu s$) ; (b) intermediate correlation time ($\tau_s = 125\,\mu s$) ; (c) long correlation time ($\tau_s = 1250\,\mu s$). The transverse velocity dispersion is $\Delta v_\perp = 0.8 m/s$, the mean saturation per beam is $s_0 = 0.04$ and the saturation fluctuation parameter is $r_s = 9\%$. The dashed exponential decay is the bare Doppler prediction (see text).

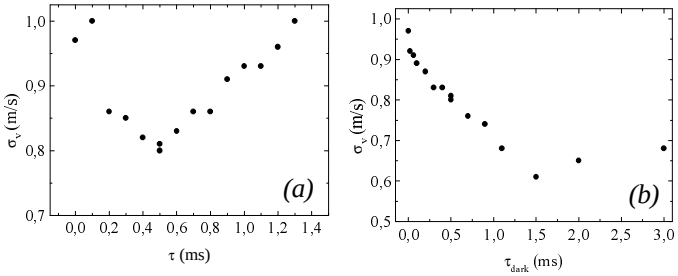

FIG. 10: (a) : Time evolution of the velocity dispersion σ_v after a dark time window of duration $\tau_{dark} = 0.5\,ms$; (b) MOT velocity dispersion σ_v as a function of the dark window duration. The dark window starts $0.5\,ms$ after the beginning of the cooling sequence (see text).